The distribution of deuterated formaldehyde within Orion–KL

Cécile Favre, Edwin A. Bergin, Justin L. Neill,

Department of Astronomy, University of Michigan, 500 Church St.,

`cfavre@umich.edu`

Ann Arbor, MI 48109, USA

and

Nathan R. Crockett

California Institute of Technology, Division of Geological and Planetary Sciences, MS 150-21, Pasadena, CA 91125, USA

and

Qizhou Zhang

Harvard-Smithsonian Center for Astrophysics, 60 Garden Street, Cambridge MA 02138, USA

and

Dariusz C. Lis

LERMA, Observatoire de Paris, PSL Research University, CNRS, Sorbonne Universités, UPMC Univ. Paris 06, F-75014, Paris, France

Cahill Center for Astronomy and Astrophysics 301–17, California Institute of Technology, Pasadena, CA 91125, USA

ABSTRACT

We report the first high angular resolution imaging ($3.4'' \times 3.0''$) of deuterated formaldehyde (HDCO) toward Orion–KL, carried out with the Submillimeter Array (SMA). We find that the spatial distribution of the formaldehyde emission systematically differs from that of methanol: while methanol is found towards the inner part of the region, HDCO is found in colder gas that wraps around the methanol emission on four sides. The HDCO/H_2CO ratios are determined to be 0.003–0.009 within the region, up to an order of magnitude higher than the D/H measured for methanol. These findings strengthen the previously suggested hypothesis that there are differences in the chemical pathways leading to HDCO (via deuterated gas phase chemistry) and deuterated methanol (through conversion of formaldehyde into methanol on the surface of icy grain mantles).

Subject headings: line: identification — astrochemistry — ISM: abundances — ISM: individual objects (Orion KL) — ISM: molecules

1. Introduction

The Orion–KL nebula, that lies at a distance of 414±7 pc (Menten et al. 2007) is a focal source for studies of the physics and chemistry of high–mass star forming regions. Its rich molecular diversity and complex physical structure have been revealed by a number of spectral line surveys and interferometric studies of the region (e.g. Blake et al. 1987; Comito et al.

2005; Schilke et al. 1997, 2001; Beuther et al. 2005, 2006; Persson et al. 2007; Guélin et al. 2008; Friedel & Snyder 2008; Tercero et al. 2010, 2011; Favre et al. 2011a,b, 2014; Brouillet et al. 2013; Peng et al. 2013; Friedel & Snyder 2008; Friedel & Widicus Weaver 2012; Widicus Weaver & Friedel 2012; Esplugues et al. 2013). Recently, a broad-band spectral line survey of Orion–KL carried out with the Herschel/HIFI spectrometer (Bergin et al. 2010; Crockett et al. 2010, 2014) has been obtained as part of the HEXOS key program[1]. The unprecedented 1.2 THz wide frequency coverage of this survey has allowed for strong constraints on physical parameters and molecular abundances due to the detection of many transitions for each molecule, with a wide range of excitation conditions, revealing the presence of thermal gradients (e.g. Wang et al. 2011). Among the molecular components associated with Orion–KL lie the so-called Hot Core and Compact Ridge. Although the precise nature of these regions remains enigmatic, evidence has been recently provided that they may have originated from the interaction of the remnants of a recent explosion with ice grains mantles ($\leq$720 years ago, e.g. Bally et al. 2011; Gómez et al. 2005, 2008; Rodríguez et al. 2005; Nissen et al. 2012), leading to the evaporation and the heating of organic material (Favre et al. 2011a; Zapata et al. 2011).

Deuterium fractionation is intrinsically a low-temperature process. Therefore, deuterated molecules in warm (T$\geq$100K) region, such as Orion-KL, offer a window into its physical conditions at the earlier, colder stage (T$\sim$10–30 K) when this material likely formed (Blake et al. 1987; Charnley et al. 1997; Pagani et al. 1992). Numerous deuterated species have been observed toward Orion–KL: deuterated water (Turner et al. 1975; Jacq et al. 1990; Neill et al. 2013b), deuterated ammonia (Rodriguez Kuiper et al. 1978; Walmsley et al. 1987), deuterated formaldehyde (Loren & Wootten 1985; Turner 1990) and deuterated methanol (Mauersberger et al. 1988; Jacq et al. 1993; Peng et al. 2012). Recently, Neill et al. (2013a) used the HIFI survey, and tens of transitions, to set strong constraints in the D/H ratio of organics associated with Orion–KL. Their finding strongly suggests that D/H fractionation is inhomogenuous in this source.

In this study, we extend the HIFI study of deuterated species performed by Neill et al. (2013a,b); especially since the Herschel observations are spatially unresolved, so even with well determined column densities within the beam, there can be large deviations in the deuterium fractionation as a function of spatial position. In Section 2, we present the SMA observations to complement the HIFI analysis. In particular, we focus on formaldehyde (H_2CO and HDCO). The D/H ratios of this molecule is key to obtaining a full picture of the oxygen chemistry in this region, as formaldehyde is believed to be an intermediate in the grain–surface synthesis of methanol through sequential reactions of H or D atoms with CO (see Watanabe & Kouchi 2002; Cazaux et al. 2011; Taquet et al. 2012). Alternatively, gas phase chemistry might independently lead to the formation of formaldehyde via reactions involving CH_2D^+ products under warmer conditions (typically T$>$ 50K, see Wootten 1987; Loren & Wootten 1985). Incidentally, the tentative detection of the CH_2D^+ ion toward Orion-KL by Roueff et al. (2013) suggests that gas phase chemistry might be efficient for the HDCO formation. In this analysis we present the first high angular resolution image of the spatial distribution of (deuterated) formaldehyde in Orion–KL and discuss the different chemical pathways that can be involved in its formation. More specifically, results and analysis are presented in Section 3 and discussed in Section 4, with conclusions set out in Section 5.

2. Observations and data reduction

Observations of Orion-KL were carried out with the SMA[2] (Ho et al. 2004) in its compact configuration on December 12, 2013 for about 6.75h. The phase-tracking centre was α_{J2000} = $05^h35^m14\overset{s}{.}20$, δ_{J2000} = -05°22′33″00. The new broader-bandwidth SMA capability of the 230 GHz band was used to cover the following frequency ranges: 192.6–194.6 GHz and 197.6–

199.6 GHz in LSB band and, 207.6–209.6 GHz and 212.6–214.6 GHz in the USB band. An enormous advantage of this broadband capability is the possibility to observe transitions of both HDCO and $H_2^{13}CO$ in a single tuning (see Table 1). The correlator was configured with a uniform spectral resolution over 4 GHz bandwidth in each sideband. Each 4 GHz bandwidth is divided into 48 'chunks', each is further divided into 128 channels with a channel width of 0.812 MHz. The weather conditions were good and stable with an atmospheric opacity of about 0.14 at 225 GHz. The SMA data were calibrated using the MIR/IDL package[3] (Qi 2007). The nearby quasars $0423-013$ and $0510+180$ were used as complex gain (phase and amplitude) calibrators.

Continuum subtraction and data imaging were performed using the MIRIAD software package. The final continuum emission maps obtained at 198 GHz and 213 GHz are shown in Figure 1. They were restored using a robust weighting of 0.0, resulting in a synthesized beam size of $3.5'' \times 3.01''$(P.A. = 32.7°) at 198 GHz and of $3.2'' \times 2.8''$(P.A. = 26.7°) at 213 GHz. Positions of the four main continuum sources derived from Gaussian fits in the (u, v) LSB dataset image plane are given in Figure 1. Positions of these continuum sources are commensurate between the LSB and USB data sets and, in agreement, within the synthesized beam size, with previous PdBI observations (Favre et al. 2011a).

In this analysis, we only focus on 2 emission lines of HDCO and 2 of para–$H_2^{13}CO$ (see spectroscopic parameters listed in Table 1). The spectral resolution is 1.14 km s^{-1} for $H_2^{13}CO$ at 212/213 GHz and 1.26 km s^{-1} for the HDCO lines at 193 GHz. The resulting synthesized beam sizes ($\sim 3'' \times 3''$, P.A. = 30 °) are given in Table 1 at the different frequencies.

3. Results and analysis

3.1. Emission maps and velocity structure

The HDCO and $H_2^{13}CO$ emission maps integrated over the line profile are shown in Figure 2. Four main molecular emission peaks, labeled dF1 to dF4, are associated with the HDCO emission. More specifically, they are located to-

ward the left of Hot Core component (dF1), the north of the Compact Ridge (dF2) and in the quiescent ridge (dF3 and dF4) located south of the Compact Ridge. Their coordinates are given in Table 1. The regions dF1, dF2 and dF3 are also associated with the $H_2^{13}CO$ emission but not the dF4 one. Incidentally, it is important to note that the integrated emission map of the $H_2^{13}CO$ transition at 213293.57 MHz is strongly contaminated by the emission from an unidentified species toward the Hot Core region. This is shown in Fig. 3, which displays the integrated emission map along with the spectrum of this $H_2^{13}CO$ line; the latter being taken at the position of the contaminated emission peak.

Spectra of the formaldehyde transitions observed towards the regions dF1 to dF4 are shown in Figure 4 and the observed line parameters are summarized in Table 1. The bulk of the formaldehyde emission towards those peaks appears to lie between v_{LSR}=7.5 km s^{-1} and v_{LSR}=9.8 km s^{-1}. This result is consistent with the HDCO LSR velocity derived by Loren & Wootten (1985) toward the quiescent ridge ($\sim$8.5 km s^{-1}, single-dish Millimeter Wave Observatory observations) and by Neill et al. (2013a) toward the region ($\sim$8 and 10.4 km s^{-1}, Herschel/HIFI observations). It is important to note that Neill et al. (2013a) have associated the HDCO emission with two velocity components in Compact Ridge. This difference results from the fact that $i)$ some complex molecules, such as methyl formate or dimethyl ether, are seen with two distinct velocity components emitting at $\sim$7.5 and 9.2 km s^{-1} in the Compact Ridge (e.g. Favre et al. 2011a; Brouillet et al. 2013) and that, $ii)$ the Herschel observations are spatially unresolved. We infer that the two HDCO velocity components seen by Neill et al. (2013a), actually correspond to our HDCO emission observed toward dF3 and dF1, respectively.

3.2. Excitation temperature

Assuming optically thin emission, we use the integrated line intensity measurements of the observed $H_2^{13}CO$ transitions to derive the formaldehyde excitation temperature (T_{ex}) within Orion–

---

[3]https://www.cfa.harvard.edu/∼cqi/mircook.html

KL following Eq. 1:

$$T_{ex} = -\frac{h\nu}{k_B \ln\left(\frac{g_l A_l \nu_u^2 W_u}{g_u A_u \nu_l^2 W_l}\right)} = -\frac{E_u - E_l}{\ln\left(\frac{g_l A_l \nu_u^2 W_u}{g_u A_u \nu_l^2 W_l}\right)}, \quad (1)$$

where E, W, A, g and ν refer to the state energies (K), the integrated line intensities (K km s^{-1}), the Einstein A coefficients (s^{-1}), the statistical weights and the line frequencies (Hz) of the $3_{2,1}$–$2_{2,0}$ (u) and $3_{0,3}$–$2_{0,2}$ (l) transitions. It is important to note that Equation 1 cannot be directly applied to HDCO since both of the detected transitions have the same upper energy level (see Table 1). Thus, the below analysis hinges upon the assumption that T_{ex} is the same for both HDCO and H$_2$^{13}CO.

Figure 5a presents the excitation temperature map for H$_2$^{13}CO within Orion-KL. The formaldehyde excitation temperature derived toward the dF2, dF3 and dF4 peaks is low (52–57 K, see Table 1) contrary to dF1, for which it is higher ($\sim$90 K). Our derived temperatures in the quiescent ridge (i.e regions dF3 and dF4) are commensurate within the uncertainties, with the one derived by Bergin et al. (1994, 60$\pm$30 K) using CH$_3$C$_2$H, a known tracer of ambient ridge gas. Regarding the dF2 emission peak, our derived temperature is in agreement with one of the KL–W methanol clump that lies in its vicinity (i.e $\sim$2″ east, see Peng et al. 2012). As for the dF1 emission peak, there is a slight discrepancy with the temperature derived by Peng et al. (2012). In particular, these authors report a temperature that is lower than the typical temperature derived in the vicinity of this region ($\sim$100–300 K, e.g. Favre et al. 2011a; Goddi et al. 2011a; Friedel & Snyder 2008). However, looking at their Figure B.4., a 130 K temperature seems to be consistent with their data, suggesting that their error bars might have been underestimated. Overall the temperatures derived here are lower than the typical temperatures derived for organic species towards the Hot Core and Compact Ridge components associated with the inner part of Orion–KL (e.g. Crockett et al. 2014).

3.3. Column density

Assuming that *i)* LTE is reached, which implies that the excitation temperature is equal to the rotational temperature and, *ii)* the rotational temperature is the same for both HDCO and H$_2$^{13}CO, we derive the total column density, N, by using the following equation (Goldsmith & Langer 1999):

$$\ln\left(\frac{8\pi k_B \nu^2 W}{g_u hc^3 A_{ul}}\right) = \ln\left(\frac{N}{Q}\right) - \frac{E_u}{T}, \quad (2)$$

where,

W	is the integrated line intensity (K cm s^{-1}),
ν	the line frequency (Hz),
A_{ul}	the Einstein coefficient (s^{-1}),
g_u	the statistical weight,
N	the total column density (cm^{-2}),
Q	the partition function,
E_{up}	the upper state energy (K),
h	the Planck constant (erg s),
k_B	the Boltzmann constant (erg/K),
c	the speed of light (cm s^{-1}), and
T	the excitation temperature derived above (in K, Sect. 3.2).

The column densities derived toward the regions dF1 to dF4 for both HDCO and para–H$_2$^{13}CO are listed in Table 1. In addition, Table 2 gives the total column densities for HDCO, H$_2$^{13}CO and H$_2$CO toward the dF1 to dF4 peaks. The total column densities have been calculated as follow: *i)* the column densities derived for the two HDCO transitions, that are listed in Table 1, have been averaged. The same applies to the two para–H$_2$^{13}CO transitions. *ii)* Regarding H$_2$^{13}CO and HDCO, we assume an ortho:para ratio of 3:1, that is commensurate with measurements performed towards Orion–KL by Kahane et al. (1984) and Crockett et al. (2014), and a ^{12}C/^{13}C isotopic ratio of 70 (see, Favre et al. 2014, and reference therein), that is in agreement within the error bars with previous studies (e.g. Persson et al. 2007; Stahl et al. 2008).

3.4. D/H ratios for formaldehyde

Using the total column densities for HDCO and for H$_2$^{13}CO (see Section 3.3 and Table 2), we derive the D/H ratio for the regions dF1 to dF4. The resulting D/H ratios are given in Table 2. Figure 5b shows the distribution map of the D/H ratio for formaldehyde in Orion–KL. The HDCO/H$_2$CO ratio is found to be 0.009$\pm$0.002 toward dF4, 0.003$\pm$0.001 toward dF1 and 0.004$\pm$0.001 and

0.005±0.002 toward dF2 and dF3, respectively. Our results are commensurate within the uncertainties with previous D/H ratio measurements in the region (e.g. Loren & Wootten 1985; Neill et al. 2013a) and suggest a possible gradient in the HDCO/$H_2{}^{13}CO$ ratio at a 3σ level.

4. Discussion

4.1. Anticorrelation between formaldehyde and methanol emission

A recent study by Peng et al. (2012) using the Plateau de Bure interferometer derived the D/H ratios of methanol (CH_2DOH and CH_3OD) at comparable resolution to our SMA observations. A notable result is that the spatial distribution of formaldehyde emission (HDCO and $H_2{}^{13}CO$, see Fig. 2) clearly differs from that of (deuterated) methanol (see Fig. 3 of Peng et al. 2012). The methanol distribution follows a V-shaped structure linking the Hot Core component to the Compact Ridge (Peng et al. 2012) while formaldehyde exhibits a spatial structure which appears to surround this molecular V-shaped structure on four sides. This difference is illustrated in Figure 2 (bottom right panel) in which the deuterated methanol emission peaks identified by Peng et al. (2012) are indicated on the HDCO integrated emission map at at 193391.6 MHz. Furthermore, the D/H ratio for methanol derived by Peng et al. (2012) lies in the range 0.8–1.3×10^{-3}, which is up to an order of magnitude (within the uncertainties) lower than the D/H ratio for formaldehyde derived in this study (see Table 2).

4.2. Origin of formaldehyde emission

All the nearby well–characterized sources (i.e. Hot Core, Compact Ridge) are not coincident with formaldehyde emission. In fact, it is possible and even likely that we are seeing quiescent material surrounding the hotter sources, such as the well–known quiescent ridge in Orion–KL. Incidentally, the spatial difference between the formaldehyde and methanol emission has already been observed toward others sources, such as the Horsehead Photon-Dominated Region (PDR) and its associated dense core (Guzmán et al. 2013) and the Orion Bar PDR (Leurini et al. 2006, 2010). In their respective analyses, the authors have shown that the UV radiation field affects the gas–
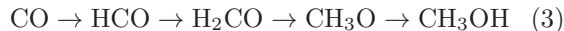
phase abundance of formaldehyde and methanol. More specifically, the H_2CO/CH_3OH abundance ratio is expected to be higher in high FUV illuminated environments in comparison to denser and less illuminated regions. In this light, the entire Orion–KL quiescent ridge gas is a face–on PDR (see Lerate et al. 2008; Persson et al. 2007; Irvine et al. 1987), therefore photodissociation of gas-phase methanol into formaldehyde might occur (e.g. see, Le Teuff et al. 2000; Leurini et al. 2006, 2010). In this context we determine the abundance ratio of H_2CO/CH_3OH in the formaldehyde clumps. Comparison to ratios measured towards other PDRs would then illuminate whether the Orion PDR is influencing the local chemistry of dense material surrounding the hot embedded cores.

The determination of the methanol column density (see Eq. 2) relies on the assumptions that the CH_3OH–E transitions listed in Table 3 are optically thin and, that the rotational temperature is the same as that of $H_2{}^{13}CO$. It is important to note that toward the dF1 and dF2 emission peaks the CH_3OH–E lines are strongly blended (see Figure 6), preventing us from deriving the column density of methanol at those positions. Regarding the dF3 and dF4 regions, the resulting H_2CO/CH_3OH abundance ratio lies in the range 3.5–4.5, that might suggest a slight decrease in the methanol abundance in the quiescent ridge. However, our derived ratio is lower by at least a factor of 3–400 in comparison to that estimated by Leurini et al. (2010) toward the Orion Bar, suggesting that the production of formaldehyde in Orion–KL through photodissociation of gas-phase methanol is not the main formation route. Finally, it is noticeable that our estimated H_2CO/CH_3OH abundance ratio is more consistent with that found in hot–corino regions (see Maret et al. 2004, 2005 and Guzmán et al. 2013 for a review). This finding leads us to argue that formaldehyde emission in Orion–KL is more likely probing the edge of the hot gas.
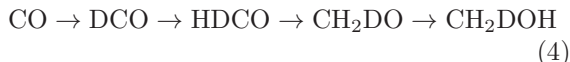
4.3. Implications: on the formaldehyde formation

Formaldehyde and methanol are believed to be formed on ice grain mantles during the prestellar cold phase (T<50 K) from successive hydrogenation reactions of H– or D– atoms with CO

(see e.g. Charnley et al. 1997; Cazaux et al. 2011; Taquet et al. 2012; Watanabe & Kouchi 2002):

$$CO \rightarrow HCO \rightarrow H_2CO \rightarrow CH_3O \rightarrow CH_3OH \quad (3)$$

and

$$CO \rightarrow DCO \rightarrow HDCO \rightarrow CH_2DO \rightarrow CH_2DOH \quad (4)$$

Laboratory experiments have shown that the sequential CO hydrogenation process (i.e. reaction 3) efficiently form both formaldehyde and methanol at low temperatures ($\leq$20 K, see Fuchs et al. 2009; Watanabe et al. 2004; Hidaka et al. 2004). Thus, if methanol and formaldehyde both purely originate from ice grain mantles, the measured D/H ratio should be similar (within a factor 2) for both molecules and, in particular, these molecules should trace similar environments while desorbed as they share a common origin. This is inconsistent with our observations (see Section 4.1) and thus strongly argues in favor of differences in the chemical formation pathways of these deuterated molecules. Thus CH_3OH and H_2CO emission is probing different spatial regions within the central region of Orion KL that may not be coeval. We infer that a likely scenario is a HDCO production through hot gas-phase deuterium chemistry in the colder gas associated with Orion–KL, as suggested by Loren & Wootten (1985). More specifically, at **relatively** high temperature (T$\sim$70K–100K, Öberg et al. 2012; Wootten 1987), such as that derived in this study (see Figure 5), reaction 5 is active due to its high exothermicity (ΔE of 654 K, see Roueff et al. 2013) and favors deuterium fractionation through reactions involving CH_2D^+ as a parent molecule (Favre et al. 2015).

$$CH_3^+ + HD \leftrightarrows CH_2D^+ + H_2 + \Delta E \quad (5)$$

In that context, reaction 5 can then lead to the formation of HDCO and H_2CO (see further details in Loren & Wootten 1985). Incidentally, the temperature of this colder region associated with Orion-KL is not sufficient enough to desorb CH_3OH from the surface of icy grain mantles (T$\geq$120–160 K see, Collings et al. 2004; Green et al. 2009). However, in the inner hottest part of Orion–KL where methanol emits, most of the formaldehyde might have been converted into methanol by grain surface reactions (Watanabe & Kouchi 2002) during a colder phase prior to the explosive event. Then, upon heating methanol is released from grain surfaces into gas phase along with little formaldehyde. We stress that the release of methanol into gas–phase in this region is mainly due to internal radiation heating (i.e outflow, shock, IR sources) but not heat from the PDR (see Section 4.2). In this instance, the D/H ratio and the spatial distribution of methanol should differ from the one of formaldehyde.

5. Conclusions

We have characterized, for the first time, the spatial distribution of deuterated formaldehyde (HDCO) toward Orion–KL with an angular resolution of $3.4'' \times 3.0''$ using the SMA. The new SMA broadband capability of the 230 GHz band allowed simultaneous observation of both HDCO and $H_2{}^{13}CO$ within relatively sparse spectra. Four main emission peaks, labelled in this study dF1 to dF4, are identified in the formaldehyde emission image. A salient result is that the spatial distribution the emission of the HDCO and $H_2{}^{13}CO$ emission differ from that of CH_3OH and its deuterated isotopologues. The emission maps show that methanol emits in the inner part of Orion–KL, while formaldehyde is found in the colder gas enveloping the CH_3OH emission on four sides: one located left of the Hot Core (dF1), one toward the north of the Compact Ridge (dF2) and two in the quiescent ridge (dF3 and dF4). In addition, we derive a HDCO/H_2CO ratio which lies in the range of 0.003 to 0.009 within the region; this value is an order of magnitude higher than the D/H measured for methanol. We suggest that the high measured D/H ratio for formaldehyde and its spatial distribution in Orion–KL are a combination of gas phase chemistry in the cooler gas associated with Orion–KL and, a conversion of formaldehyde into methanol on ice grain mantles in the earlier history of the inner part.

Facilities: SMA

REFERENCES

Bally, J., Cunningham, N. J., Moeckel, N., et al. 2011, ApJ, 727, 113

Bergin, E. A., Goldsmith, P. F., Snell, R. L., & Ungerechts, H. 1994, ApJ, 431, 674

Bergin, E. A., Phillips, T. G., Comito, C., et al. 2010, A&A, 521, L20

Beuther, H., Zhang, Q., Greenhill, L. J., et al. 2005, ApJ, 632, 355

Beuther, H., Zhang, Q., Reid, M. J., et al. 2006, ApJ, 636, 323

Blake, G. A., Sutton, E. C., Masson, C. R., & Phillips, T. G. 1987, ApJ, 315, 621

Bocquet, R., Demaison, J., Cosléou, J., et al. 1999, Journal of Molecular Spectroscopy, 195, 345

Brouillet, N., Despois, D., Baudry, A., et al. 2013, A&A, 550, A46

Cazaux, S., Caselli, P., & Spaans, M. 2011, ApJ, 741, L34

Charnley, S. B., Tielens, A. G. G. M., & Rodgers, S. D. 1997, ApJ, 482, L203

Collings, M. P., Anderson, M. A., Chen, R., et al. 2004, MNRAS, 354, 1133

Comito, C., Schilke, P., Phillips, T. G., et al. 2005, ApJS, 156, 127

Crockett, N. R., Bergin, E. A., Wang, S., et al. 2010, A&A, 521, L21+

Crockett, N. R., Bergin, E. A., Neill, J. L., et al. 2014, ApJ, 787, 112

Esplugues, G. B., Tercero, B., Cernicharo, J., et al. 2013, A&A, 556, A143

Favre, C., Bergin, E. A., Cleeves, L. I., et al. 2015, ApJ, 802, L23

Favre, C., Despois, D., Brouillet, N., et al. 2011a, A&A, 532, A32

Favre, C., Wootten, H. A., Remijan, A. J., et al. 2011b, ApJ, 739, L12

Favre, C., Carvajal, M., Field, D., et al. 2014, ApJS, 215, 25

Friedel, D. N., & Snyder, L. E. 2008, ApJ, 672, 962

Friedel, D. N., & Widicus Weaver, S. L. 2012, ApJS, 201, 17

Fuchs, G. W., Cuppen, H. M., Ioppolo, S., et al. 2009, A&A, 505, 629

Goddi, C., Greenhill, L. J., Humphreys, E. M. L., Chandler, C. J., & Matthews, L. D. 2011a, ApJ, 739, L13

Goddi, C., Humphreys, E. M. L., Greenhill, L. J., Chandler, C. J., & Matthews, L. D. 2011b, ApJ, 728, 15

Goldsmith, P. F., & Langer, W. D. 1999, ApJ, 517, 209

Gómez, L., Rodríguez, L. F., Loinard, L., et al. 2008, ApJ, 685, 333

—. 2005, ApJ, 635, 1166

Green, S. D., Bolina, A. S., Chen, R., et al. 2009, MNRAS, 398, 357

Guélin, M., Brouillet, N., Cernicharo, J., Combes, F., & Wooten, A. 2008, Ap&SS, 313, 45

Guzmán, V. V., Goicoechea, J. R., Pety, J., et al. 2013, A&A, 560, A73

Hidaka, H., Watanabe, N., Shiraki, T., Nagaoka, A., & Kouchi, A. 2004, ApJ, 614, 1124

Ho, P. T. P., Moran, J. M., & Lo, K. Y. 2004, ApJ, 616, L1

Irvine, W. M., Goldsmith, P. F., & Hjalmarson, A. 1987, Astrophysics and Space Science Library, Vol. 134, Chemical abundances in molecular clouds, ed. D. J. Hollenbach & H. A. Thronson Jr., 561–609

Jacq, T., Walmsley, C. M., Henkel, C., et al. 1990, A&A, 228, 447

Jacq, T., Walmsley, C. M., Mauersberger, R., et al. 1993, A&A, 271, 276

Johns, J. W. C., & McKellar, A. R. W. 1977, Journal of Molecular Spectroscopy, 64, 327

Kahane, C., Lucas, R., Frerking, M. A., Langer, W. D., & Encrenaz, P. 1984, A&A, 137, 211

Le Teuff, Y. H., Millar, T. J., & Markwick, A. J. 2000, A&AS, 146, 157

Lerate, M. R., Yates, J., Viti, S., et al. 2008, MNRAS, 387, 1660

Leurini, S., Parise, B., Schilke, P., Pety, J., & Rolffs, R. 2010, A&A, 511, A82

Leurini, S., Rolffs, R., Thorwirth, S., et al. 2006, A&A, 454, L47

Loren, R. B., & Wootten, A. 1985, ApJ, 299, 947

Maret, S., Ceccarelli, C., Tielens, A. G. G. M., et al. 2005, A&A, 442, 527

Maret, S., Ceccarelli, C., Caux, E., et al. 2004, A&A, 416, 577

Mauersberger, R., Henkel, C., Jacq, T., & Walmsley, C. M. 1988, A&A, 194, L1

Menten, K. M., Reid, M. J., Forbrich, J., & Brunthaler, A. 2007, A&A, 474, 515

Müller, H. S. P., Schlöder, F., Stutzki, J., & Winnewisser, G. 2005, Journal of Molecular Structure, 742, 215

Müller, H. S. P., Gendriesch, R., Margulès, L., et al. 2000, Physical Chemistry Chemical Physics (Incorporating Faraday Transactions), 2, 3401

Neill, J. L., Crockett, N. R., Bergin, E. A., Pearson, J. C., & Xu, L.-H. 2013a, ApJ, 777, 85

Neill, J. L., Wang, S., Bergin, E. A., et al. 2013b, ApJ, 770, 142

Nissen, H. D., Cunningham, N. J., Gustafsson, M., et al. 2012, A&A, 540, A119

Öberg, K. I., Qi, C., Wilner, D. J., & Hogerheijde, M. R. 2012, ApJ, 749, 162

Pagani, L., Salez, M., & Wannier, P. G. 1992, A&A, 258, 479

Peng, T.-C., Despois, D., Brouillet, N., Parise, B., & Baudry, A. 2012, A&A, 543, A152

Peng, T.-C., Despois, D., Brouillet, N., et al. 2013, A&A, 554, A78

Persson, C. M., Olofsson, A. O. H., Koning, N., et al. 2007, A&A, 476, 807

Qi, C. 2007, Advances in Space Research, 40, 639

Remijan, A. J., Markwick-Kemper, A., & ALMA Working Group on Spectral Line Frequencies. 2007, BAAS, 38, 963

Rodríguez, L. F., Poveda, A., Lizano, S., & Allen, C. 2005, ApJ, 627, L65

Rodriguez Kuiper, E. N., Kuiper, T. B. H., & Zuckerman, B. 1978, ApJ, 219, L49

Roueff, E., Gerin, M., Lis, D. C., et al. 2013, Journal of Physical Chemistry A, 117, 9959

Schilke, P., Benford, D. J., Hunter, T. R., Lis, D. C., & Phillips, T. G. 2001, ApJS, 132, 281

Schilke, P., Groesbeck, T. D., Blake, G. A., & Phillips, T. G. 1997, ApJS, 108, 301

Stahl, O., Casassus, S., & Wilson, T. 2008, A&A, 477, 865

Taquet, V., Ceccarelli, C., & Kahane, C. 2012, ApJ, 748, L3

Tercero, B., Cernicharo, J., Pardo, J. R., & Goicoechea, J. R. 2010, A&A, 517, A96

Tercero, B., Vincent, L., Cernicharo, J., Viti, S., & Marcelino, N. 2011, A&A, 528, A26+

Turner, B. E. 1990, ApJ, 362, L29

Turner, B. E., Fourikis, N., Morris, M., Palmer, P., & Zuckerman, B. 1975, ApJ, 198, L125

Walmsley, C. M., Hermsen, W., Henkel, C., Mauersberger, R., & Wilson, T. L. 1987, A&A, 172, 311

Wang, S., Bergin, E. A., Crockett, N. R., et al. 2011, A&A, 527, A95+

Watanabe, N., & Kouchi, A. 2002, ApJ, 571, L173

Watanabe, N., Nagaoka, A., Shiraki, T., & Kouchi, A. 2004, ApJ, 616, 638

Widicus Weaver, S. L., & Friedel, D. N. 2012, ApJS, 201, 16

Wootten, A. 1987, in IAU Symposium, Vol. 120, Astrochemistry, ed. M. S. Vardya & S. P. Tarafdar, 311–318

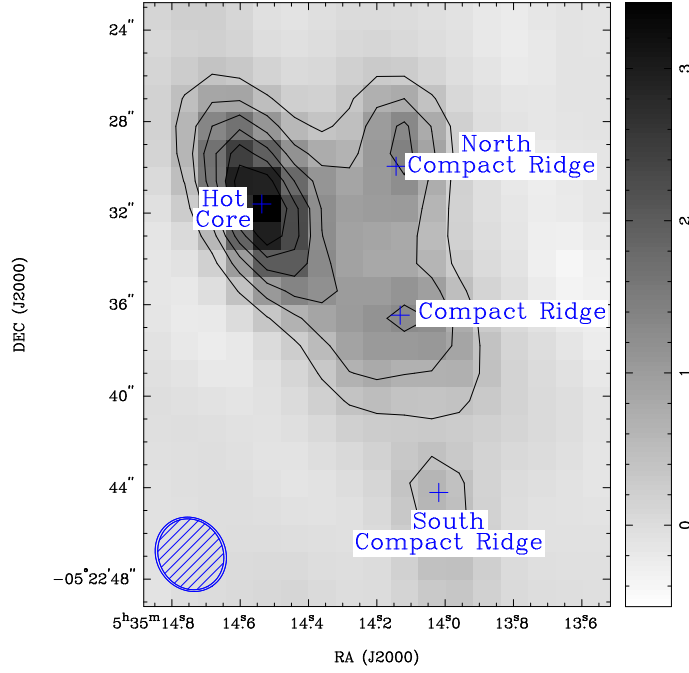Zapata, L. A., Schmid-Burgk, J., & Menten, K. M. 2011, A&A, 529, A24

Fig. 1.— Continuum emission maps obtained at 213 GHz (grey scale, USB band) and at 198 GHz (black, LSB band) toward Orion–KL as measured with the SMA. The first contour and the level step are at 3σ (where 1σ=0.132 Jy beam^{-1}). The synthesized beams are $3.2''\times 2.8''$(P.A. = 26.7°) and $3.5''\times 3.01''$(P.A. = 32.7°) at 207 GHz and 198 GHz, respectively. Blue crosses mark the positions of the four main continuum sources derived from Gaussian fits in the (u, v) plane (198 GHz dataset, LSB band). These sources are the Hot core ($\alpha_{J2000} = 05^h35^m14\overset{s}{.}537$, $\delta_{J2000} = $-05°22'31''.600), the Compact Ridge ($\alpha_{J2000} = 05^h35^m14\overset{s}{.}132$, $\delta_{J2000} = $-05°22'36''.462), the North Compact Ridge ($\alpha_{J2000} = 05^h35^m14\overset{s}{.}144$, $\delta_{J2000} = $-05°22'29''.295) and the South Compact Ridge ($\alpha_{J2000} = 05^h35^m14\overset{s}{.}019$, $\delta_{J2000} = $-05°22'44''.212).
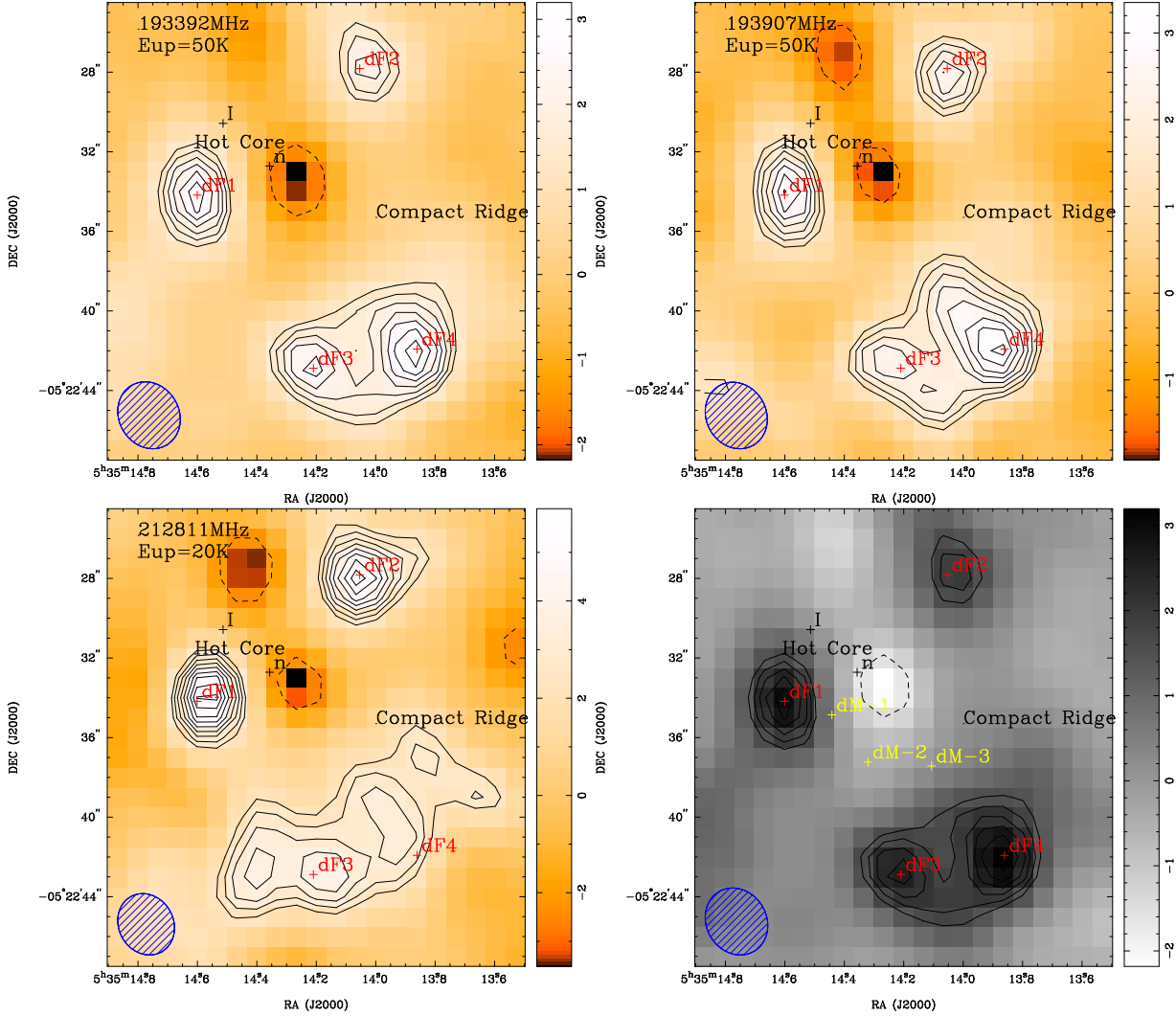
Fig. 2.— Formaldehyde integrated emission maps from v_{LSR}=6.5 km s^{-1} to v_{LSR}=10.0 km s^{-1}. Red crosses indicate the position of the regions dF1 to dF4. Black crosses indicate the positions of the radio source I ($\alpha_{J2000} = 05^h35^m14\overset{s}{.}5141$, δ_{J2000} = -05°22′30″575) and the IR source n ($\alpha_{J2000} = 05^h35^m14\overset{s}{.}3571$, δ_{J2000} = -05°22′32″719) (Goddi et al. 2011b). *Top:* HDCO emission at 193391.6 MHz (left panel) and 193907.5 MHz (right panel). *Bottom left:* H$_2^{13}$CO emission at 212811.2 MHz. The first contour is at 5σ and the level step at 1σ (where σ=0.27 and 0.44 Jy beam^{-1} km s^{-1} for HDCO and H$_2^{13}$CO, respectively). *Bottom right:* same as the top left panel, expect for deuterated methanol emission peaks (in yellow) identified by Peng et al. (2012) are indicated.
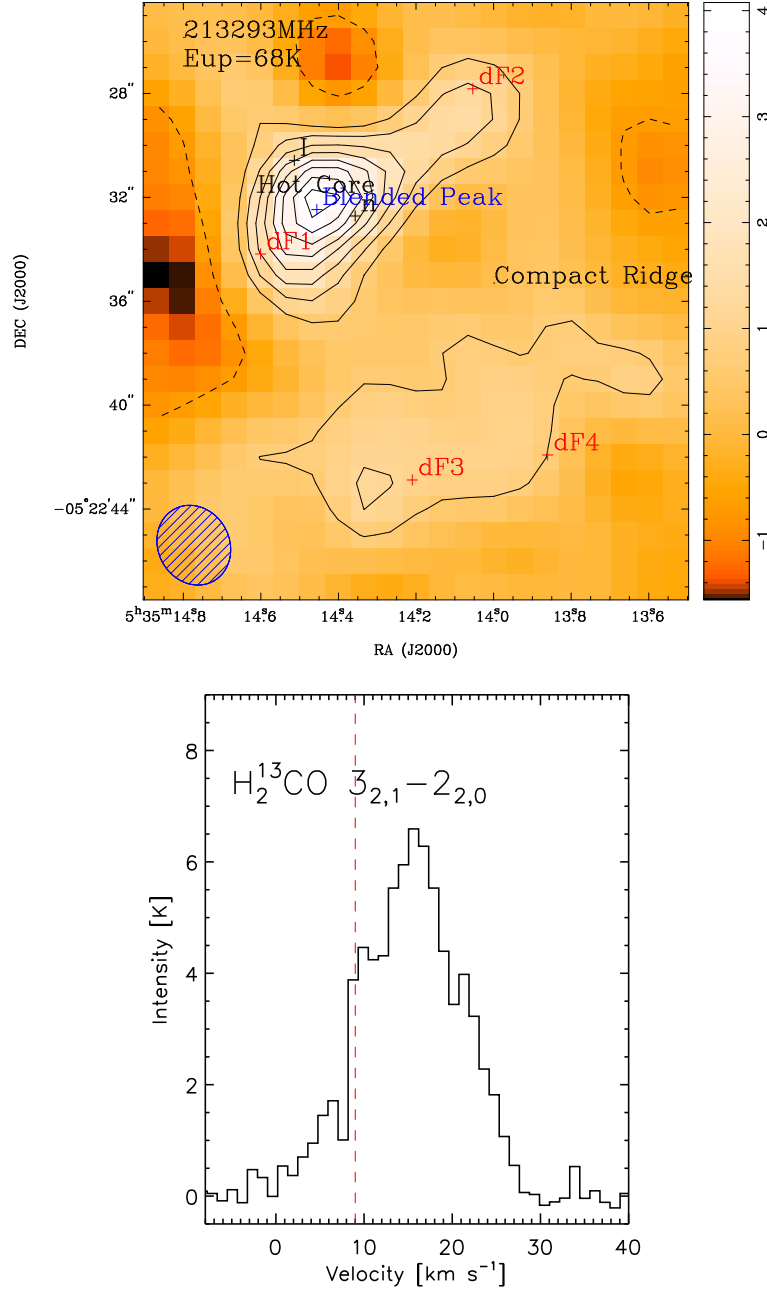
11

Fig. 3.— *Top:* $H_2^{13}CO$ integrated emission map at 213293.6 MHz from v_{LSR}=6.5 km s^{-1} to v_{LSR}=10.0 km s^{-1}. Red crosses indicate the position of the regions dF1 to dF4 while black crosses indicate the positions of the radio source I and the IR source n (see Fig. 2). The first contour is at 3σ and the level step at 2σ (where σ=0.27 Jy beam^{-1} km s^{-1}). The emission of this $H_2^{13}CO$ transition is strongly contaminated by the emission from an unidentified species toward the Hot Core region marked by a blue cross and labelled "Blended Peak". *Bottom:* $H_2^{13}CO$ spectrum observed towards the "Blended Peak" position (blue cross). The red dashed line indicates a LSR velocity of 9.0 km s^{-1}.
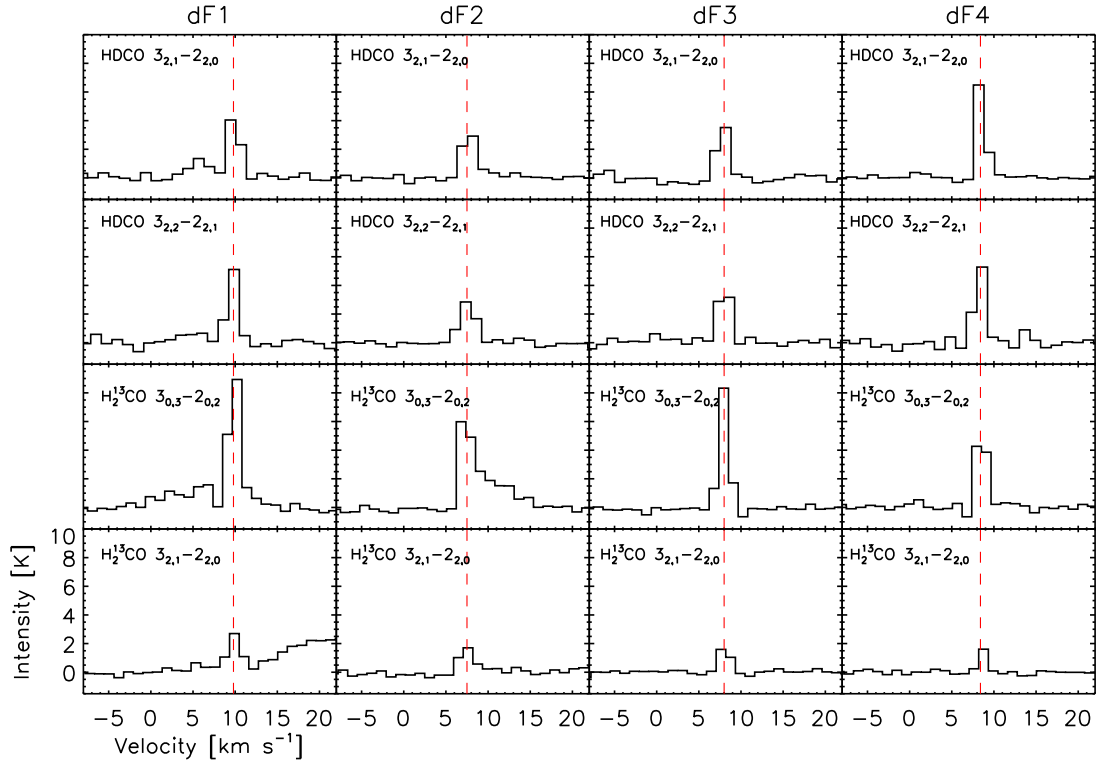
Fig. 4.— HDCO and $H_2^{13}CO$ spectra observed towards dF1, dF2, dF3 and dF4. The red dashed line indicates the v_{LSR} towards each peak (i.e 9.8, 7.5, 8.0 and 8.4 km s^{-1}, respectively).
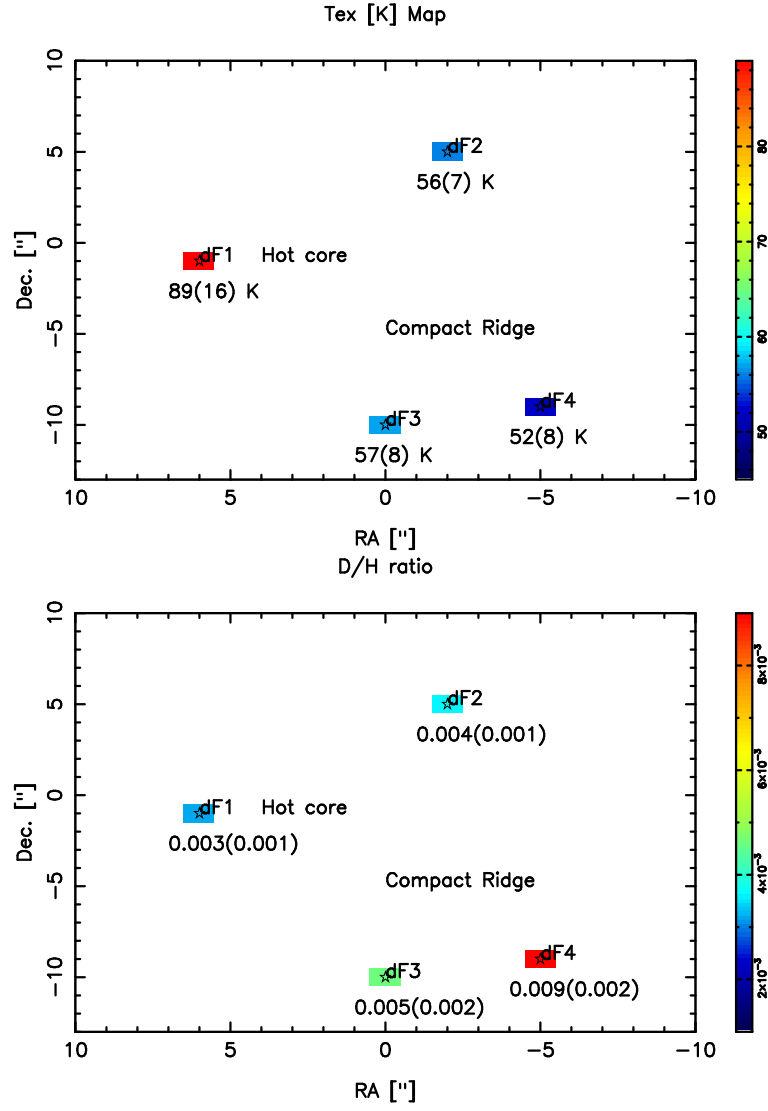
Fig. 5.— *Top:* H$_2^{13}$CO excitation temperature map toward Orion-KL. *Bottom:* D/H ratio for formaldehyde within Orion–KL.
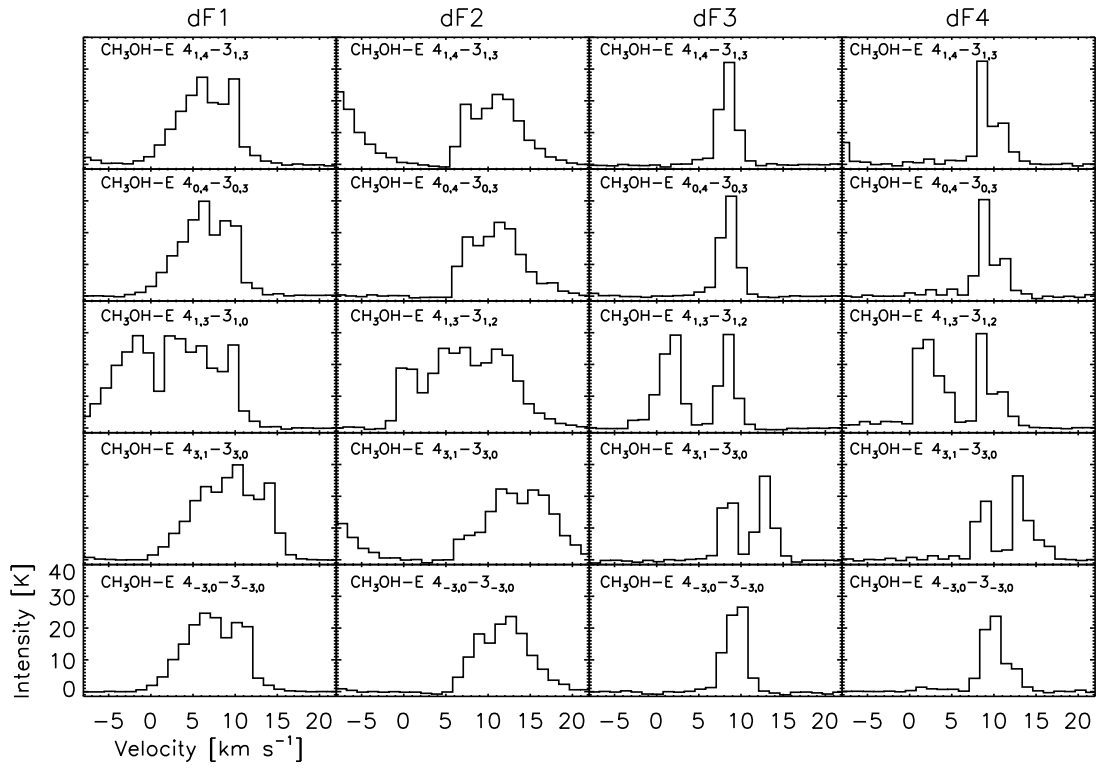
Fig. 6.— CH$_3$OH–E spectra observed towards dF1, dF2, dF3 and dF4.

TABLE 1

SPECTROSCOPIC AND OBSERVATIONAL LINE PARAMETERS FOR FORMALDEHYDE[a,b]

HDCO

Frequency (MHz)	Transition	E_{up} (K)	A ×10⁻⁴ (s⁻¹)	Synthesized beam ('' × '')	PA (°)	dF1 ∫T_{mb}dv (K km s⁻¹)	v_{LSR} (km s⁻¹)	Δv_{LSR} (km s⁻¹)	T_{ex} (K)	N (10¹⁴cm⁻²)	dF2 ∫T_{mb}dv (K km s⁻¹)	v_{LSR} (km s⁻¹)	Δv_{LSR} (km s⁻¹)	T_{ex} (K)	N (10¹⁴cm⁻²)
192893.26[c]	$3_{0,3}-2_{0,2}$	18.5	1.94	–	–	–	–	–	–	–	–	–	–	–	–
193907.46	$3_{2,1}-2_{2,0}$	50.4	1.10	3.44 × 3.01	30	8.50(1.54)	9.84(0.14)	1.80(0.46)	89(16)	4.65(0.86)	7.38(0.43)	7.75(0.10)	2.20(0.18)	56(7)	2.92(0.22)
193391.61	$3_{2,2}-2_{2,1}$	50.4	1.09	3.47 × 3.02	30	9.05(0.63)	9.65(0.10)	1.69(0.16)	89(16)	4.96(0.37)	7.07(0.35)	7.57(0.07)	2.40(0.15)	56(7)	2.80(0.18)

Frequency (MHz)	Transition	E_{up} (K)	A ×10⁻⁴ (s⁻¹)	Synthesized beam ('' × '')	PA (°)	dF3 ∫T_{mb}dv (K km s⁻¹)	v_{LSR} (km s⁻¹)	Δv_{LSR} (km s⁻¹)	T_{ex} (K)	N (10¹⁴cm⁻²)	dF4 ∫T_{mb}dv (K km s⁻¹)	v_{LSR} (km s⁻¹)	Δv_{LSR} (km s⁻¹)	T_{ex} (K)	N (10¹⁴cm⁻²)
192893.26[c]	$3_{0,3}-2_{0,2}$	18.5	1.94	–	–	–	–	–	–	–	–	–	–	–	–
193907.46	$3_{2,1}-2_{2,0}$	50.4	1.10	3.44 × 3.01	30	7.13(0.98)	7.80(0.10)	1.71(0.32)	57(8)	2.77(0.42)	11.25(1.45)	8.61(0.05)	1.13(0.14)	52(8)	4.26(0.62)
193391.61	$3_{2,2}-2_{2,1}$	50.4	1.09	3.47 × 3.02	30	8.00(2.29)	8.00(0.03)	1.39(0.44)	57(8)	3.12(0.93)	9.79(1.02)	8.30(0.10)	1.66(0.24)	52(8)	3.71(0.45)

(para–)H₂¹³CO

Frequency (MHz)	Transition	E_{up} (K)	A ×10⁻⁴ (s⁻¹)	Synthesized beam ('' × '')	PA (°)	dF1 ∫T_{mb}dv (K km s⁻¹)	v_{LSR} (km s⁻¹)	Δv_{LSR} (km s⁻¹)	T_{ex} (K)	N (10¹⁴cm⁻²)	dF2 ∫T_{mb}dv (K km s⁻¹)	v_{LSR} (km s⁻¹)	Δv_{LSR} (km s⁻¹)	T_{ex} (K)	N (10¹⁴cm⁻²)
212811.18	$3_{0,3}-2_{0,2}$	20.4	2.64	3.17 × 2.75	30	17.99(1.73)	9.88(0.09)	1.83(0.24)	89(16)	5.44(0.53)	16.04(1.37)	7.44(0.11)	2.54(0.29)	56(7)	2.83(0.26)
213037.34[d]	$3_{2,2}-2_{2,1}$	67.7	1.46	–	–	–	–	–	–	–	–	–	–	–	–
213293.57	$3_{2,1}-2_{2,0}$	67.7	1.46	3.15 × 2.75	30	5.87(0.85)	9.89(0.19)	2.21(0.42)	89(16)	5.43(0.82)	3.84(0.40)	7.43(0.13)	2.16(0.30)	56(7)	2.83(0.35)

Frequency (MHz)	Transition	E_{up} (K)	A ×10⁻⁴ (s⁻¹)	Synthesized beam ('' × '')	PA (°)	dF3 ∫T_{mb}dv (K km s⁻¹)	v_{LSR} (km s⁻¹)	Δv_{LSR} (km s⁻¹)	T_{ex} (K)	N (10¹⁴cm⁻²)	dF4 ∫T_{mb}dv (K km s⁻¹)	v_{LSR} (km s⁻¹)	Δv_{LSR} (km s⁻¹)	T_{ex} (K)	N (10¹⁴cm⁻²)
212811.18	$3_{0,3}-2_{0,2}$	20.4	2.64	3.17 × 2.75	30	12.93(0.28)	7.94(0.03)	1.55(0.04)	57(8)	2.27(0.64)	9.70(1.16)	8.44(0.03)	1.58(0.25)	52(8)	1.58(0.20)
213037.34[d]	$3_{2,2}-2_{2,1}$	67.7	1.46	–	–	–	–	–	–	–	–	–	–	–	–
213293.57	$3_{2,1}-2_{2,0}$	67.7	1.46	3.15 × 2.75	30	3.14(0.55)	8.03(0.08)	1.56(0.37)	57(8)	2.27(0.44)	2.16(0.26)	8.63(0.17)	1.30(0.23)	52(8)	1.58(0.23)

NOTE.—The HDCO emission peaks lie at the following positions: dF1 (α_{J2000}=05^{h}35^{m}14^s.601, δ_{J2000}=-05°22'34''.18), dF2 (α_{J2000}=05^{h}35^{m}14^s.054, δ_{J2000}=-05°22'27''.82), dF3 (α_{J2000}=05^{h}35^{m}14^s.210, δ_{J2000}=-05°22'42''.88) and dF4 (α_{J2000}=05^{h}35^{m}13^s.861, δ_{J2000}=-05°22'41''.92). The excitation temperature of HDCO towards those peaks is fixed and taken equal to that of H₂¹³CO as described in Section 3.2.

[a]Measured and predicted transitions are available from the CDMS (http://www.astro.uni-koeln.de/cdms/, Müller et al. 2005) database and at Splatalogue (www.splatalogue.net, Remijan et al. 2007). More specifically and as previously reported by Neill et al. (2013a), we used the spectroscopic data parameters from Müller et al. (2000) for H₂¹³CO and from Bocquet et al. (1999) and Johns & McKellar (1977) for HDCO.

[b]The numbers in brackets refer to the 1σ level uncertainty.

[c,d]These two lines have been excluded from our analysis since their emission is contaminated by the emission from HCOOCH₃ and ³³SO, respectively.

TABLE 2

TOTAL FORMALDEHYDE COLUMN DENSITIES AND D/H RATIOS

Position	N(HDCO) $(\times 10^{14} \text{cm}^{-2})$	N(H$_2{}^{13}$CO) $(\times 10^{14} \text{cm}^{-2})$	N(H$_2$CO) $(\times 10^{16} \text{cm}^{-2})$	D/H ratio
dF1	4.81(0.62)	21.70(2.72)	15.20(1.90)	0.0032(0.0008)
dF2	2.86(0.20)	11.30(1.22)	7.92(0.86)	0.0036(0.0006)
dF3	2.94(0.67)	9.06(1.00)	6.34(0.70)	0.0046(0.0016)
dF4	3.99(0.54)	6.34(0.85)	4.44(0.60)	0.0090(0.0024)

NOTE.—The total H$_2{}^{13}$CO and H$_2$CO column densities have been derived assuming an ortho:para ratio of 3:1 (e.g. see Kahane et al. 1984; Crockett et al. 2014) and a ^{12}C/^{13}C isotopic ratio of 70 (e.g. see, Favre et al. 2014).

TABLE 3

SPECTROSCOPIC PARAMETERS OF THE CH_3OH–E METHANOL TRANSITIONS OBSERVED WITH THE SMA TOWARDS THE dF3 AND dF4 EMISSION PEAKS[a]

Frequency (MHz)	Transition	E_{up} (K)	A ($\times 10^{-5}$ s^{-1})
193415.37	$4_{0,4} - 3_{0,3}\ v_t{=}0$	36.3	3.03
193441.61	$4_{1,4} - 3_{1,3}\ v_t{=}0$	28.8	2.84
193474.33	$4_{3,1} - 3_{3,0}\ v_t{=}0$	70.9	1.33
193488.99	$4_{3,2} - 3_{3,1}\ v_t{=}0$	85.9	1.33
193506.60	$4_{1,3} - 3_{1,2}\ v_t{=}0$	44.3	2.91

[a]Measured and predicted transitions are available from the CDMS database (Müller et al. 2005) and at Splatalogue (www.splatalogue.net, Remijan et al. 2007).